TRENDS IN SCIENCES 2025; 22(8): 10049
https://doi.org/10.48048/tis.2025.10049
RESEARCH ARTICLE

Production of Nanocellulose-Based Biopolymer Scaffold for Liver Tissue Engineering

Pongsatorn Poopisut[1], Sirilak Somredngan[2], Kanjana Thumanu[3], Rangsun Parnpai[1] and Apichat Boontawan[1,*]

[1]School of Biotechnology, Institute of Agricultural Technology, Suranaree University of Technology, Nakhon Ratchasima 30000, Thailand
[2]Medeze Research and Development, Medeze Group Public Company Limited, Nakhon Pathom 73220, Thailand
[3]Synchrotron Light Research Institute, Public Organization, Nakhon Ratchasima 30000, Thailand

([*]Corresponding author's e-mail: apichat@sut.ac.th)

Received: 25 February 2025, Revised: 23 March 2025, Accepted: 30 March 2025, Published: 20 June 2025

Abstract

Composite materials with tailored properties are increasingly sought after for tissue engineering applications. The aim of this work was to fabricate a nanocellulose-based biopolymer scaffold that was specifically designed for liver tissue engineering. Nanocellulose was extracted from natural sugarcane bagasse, which involved a synergistic approach that combined high-pressure homogenization (30,000 psi, 15 cycles) and enzymatic digestion (enzyme concentration: 7 %). The resulting nanocellulose exhibited an average size of 278.9 nm, a polydispersity index (PDI) of 0.752, and a crystallinity index of 50 %. This optimized nanocellulose was blended with biopolymers, polylactic acid (PLA), and polybutylene succinate (PBS) for scaffold production using film casting technique. The composite material proportions were optimized using response surface methodology (RSM), which led to an optimal composition of 65.00 wt% PLA, 26.81 wt% PBS, and 8.19 wt% nanocellulose. *In vitro* cytotoxicity evaluation of the optimized scaffold revealed a high average cell viability of 96.65 %. Human Wharton's jelly (hWJ) mesenchymal stem cells (MSCs) were seeded onto the scaffold and exhibited the potential to differentiate towards a hepatocyte lineage for 17 days. This work could be a significant initial step towards the development of novel nanocellulose-based scaffolds for applications in liver tissue engineering.

Keywords: Nanocellulose, Scaffold, Biopolymer, Tissue engineering

Introduction

The liver is the body's central organ for chemical homeostasis and regulates a vast array of blood constituents. It performs a multifaceted role in blood processing, including the breakdown, synthesis, and balanced distribution of nutrients. Additionally, the liver detoxifies medications by converting them into forms that can be readily used by the body or rendered non-toxic for excretion. The liver also plays a critical role in detoxification by producing bile, which facilitates the elimination of waste products and the emulsification of fats for efficient digestion within the small intestine.

Liver disease constitutes a significant global health burden and accounts for approximately two million deaths annually. This equivalent to 4 % of all mortalities worldwide or one out of every 25 deaths [1]. Notably, investigations have revealed a disproportionate impact on the male population, with roughly two-thirds of fatalities occurring in men [1]. However, tissue bioengineering has emerged as a promising avenue for the development of treatments. Bioengineering involves the transplantation of decellularized or recellularized hepatic scaffolds, which have primarily been applied in animal models of various hepatic lesions, such as

cirrhosis. The ultimate objective of such research is to make this technology applicable in human liver transplantation procedures [2].

Scaffolds for tissue engineering are often derived from natural sources. However, the production of biocompatible materials remains a challenge. Polylactic acid (PLA) is one of the most widely used biopolymers for tissue engineering and has advantages such as renewability, biocompatibility, and cost-effectiveness [3]. Another promising biomaterial is polybutylene succinate (PBS), which is a soft polymer that provides an excellent plasticizing effect on mechanically stiff but brittle polymers like PLA. Furthermore, PBS has recently gained attention due to its flexibility, high degree of crystallinity, and cell-friendly surface characteristics [4]. Mixing PLA with PBS enhances the performance and biocompatibility of the materials [5], and this PLA/PBS mixture can be reinforced further by adding nanocellulose.

Cellulose is the most abundant polymer derived from biomass and is composed of β-glucose molecules linked by 1,4 glycosidic bonds that form a linear homopolysaccharide. It can be extracted from plant cell walls and broken down into nanoscale fibrils known as nanocellulose. These fibrils have both highly ordered crystalline regions and disordered amorphous regions. The crystalline structure contributes to the high stiffness and strength of nanocellulose, while the amorphous regions provide flexibility. The morphology, particle size, crystallinity, and other properties of nanocellulose can vary depending on the source and extraction methods [6]. Utilizing cellulose from biomass mitigates industrial waste while enhancing the value of these byproducts, contributing to sustainable resource utilization.

Nanocellulose is typically prepared using chemical or mechanical methods. However, chemical methods can generate wastewater during the washing process. Dialysis is the main process for acid removal and nanocellulose purification, but it can be time consuming. Enzymatic hydrolysis is a biological treatment process that uses enzymes and offers a promising alternative for nanocellulose production. This method avoids hazardous waste generation, reduces water consumption, and even allows the use of released sugars as substrates in other bioprocesses [7]. The top-down production of nanocellulose through mechanical processes and enzymatic hydrolysis is faster and more productive than the bottom-up cultivation of bacterial cellulose while also contributing to the reduction of agricultural waste. Mechanical testing studies on nanocellulose-reinforced biopolymers have demonstrated significant property enhancements across various research efforts. In PLA composites, tensile strength increases by 21 % with 5 wt% cellulose nanofibrils (CNF) [8], while tensile strength achieved a 54 % improvement using 1 wt% cellulose nanocrystals (CNC) with surfactant [9]. More dramatic results were observed in modulus and strength (up to 58 and 210 %, respectively) with well-dispersed CNC [10]. However, cellulose nanofibrils CNF led to higher strength and modulus than CNC at the same fiber concentration [11]. For PBS matrices, even more substantial improvements were recorded, and tensile modulus increased with the addition of CNF or CNC [12]. Overall, these studies highlight the effectiveness of nanocellulose as a reinforcing agent for biopolymers. Relatively low concentrations of nanocellulose (typically 1 - 5 wt%) can substantially enhance mechanical properties, particularly modulus. This reinforces the potential of nanocellulose-reinforced biopolymers for various applications, including packaging, biomedical devices, and tissue engineering.

Nanocellulose have been extensively studied for their biomedical applications, with various *in vivo* studies evaluating their safety profiles. A study on cellulose nanofibrils (CNF) administered to rats over 5 weeks showed no significant toxic effects, as assessments of hematology, serum markers, and organ histology revealed no adverse changes, suggesting that ingested nanocellulose is likely non-hazardous in small quantities [13]. PLA implants typically induce mild inflammatory responses that resolve over time, though localized acidosis from degradation products remains a concern [14,15]. Similar results occurred for PBS and PBS/PLA, while in the case of PLA, the inflammation was still occurring to some extent [16]. However, Numerous *in vivo* studies on biopolymers have revealed generally favorable biocompatibility profiles with manageable side effects.

This study investigated the feasibility of using a combination of high-pressure homogenization and enzymatic hydrolysis to enhance nanocellulose production from sugarcane bagasse. The resulting

nanocellulose was used to reinforce a composite scaffold made from PLA/PBS biopolymer, which was fabricated using film casting for tissue engineering applications. Mesenchymal stem cells were cultured and differentiated into hepatocytes on the scaffold for 17 days. The chemical composition of the purified cellulose was characterized, and the average size and zeta potential were determined using a particle analyzer.

The chemical structure of the nanocellulose was analyzed using Fourier transform infrared (FTIR) spectroscopy and wide-angle X-ray scattering (WAXS) experiments. The morphologies were observed using field emission scanning electron microscopy (FESEM) and transmission electron microscopy (TEM). A cell analysis was done to test the biocompatibility and toxicity of the scaffold before cell culturing using a 3-(4,5-dimethylthiazol-2-yl)-2,5-diphenyl tetrazolium bromide (MTT) assay. The cell adhesion was confirmed using FESEM and confocal microscopy.

Materials and methods

Nanocellulose preparation

Sugarcane bagasse was obtained from the Mitr Phol Company in Thailand. Cellulose was extracted by first pretreating the bagasse with a 4 % sodium hydroxide solution (1:15 w/v ratio) for 24 h at 60 °C. The pretreated was then washed with reverse osmosis (RO) water until it reached neutral pH. To remove color from the sample, the bagasse was placed in a 15 % hydrogen peroxide solution (1:10 ratio) at 80 °C for 2 h, followed by another wash in RO water until pH 7 was achieved. This method was adapted for sugarcane bagasse pretreatment [17]. The wet cellulose was dried overnight at 50 °C in a tray dryer, mashed, and passed through a 50-µm sieve. A 1 % cellulose mixture was prepared by sieving the cellulose with RO water before size reduction.

A hydraulic pilot-scale homogenizer (Microfluidics, M-110EH-30, USA) was operated using various pressures (10,000 - 30,000 psi) in combination with an enzymatic process for nanocellulose production. A commercial enzyme cocktail (Novozymes, C-Tech 2, Denmark) was added to the cellulose powder at 1 - 7 % w/w, and the mixture was incubated at 50 °C for 96 h to promote size reduction. The enzymatic hydrolysis was stopped by boiling for 5 min. The resulting nanocellulose was then centrifuged at 8,000 rpm for 30 min at 25 °C and washed 3 times before being transferred to a spray dryer. Finally, the nanocellulose was dried using a mini spray dryer (Buchi, B-250, Switzerland) with an inlet temperature of 130 °C, air flow rate of 470 L/h, feed rate of 3.5 mL/min, nozzle size of 1.4 mm, and aspirator pressure drop of −50 mbar.

Production of nanocellulose based biopolymer scaffold

Design-Expert software version 13 was used to optimize the polymer ratio using the mixture design model. The model was operated using the following constraints: 65 % ≤ PLA ≤ 90 %, PBS ≤ 35 %, cellulose ≤ 10 %, PBS + cellulose ≤ 40 %, and PLA + PBS + cellulose = 100 %. The details of the designed experiment are presented in **Table 1**. The measured responses included the water contact angle, medium contact angle, and maximum tensile force.

The composite materials were dissolved in N-methyl pyrrolidone (NMP) at 150 °C at a total polymer concentration of 30 wt%. Scaffolds were then fabricated using the film casting technique. Immediately after casting, the scaffolds were immersed in a solution to remove the solvent, which was repeated twice. The wet scaffolds were left at room temperature for a few minutes before drying overnight at 50 °C. The prepared scaffolds were 8 mm in diameter and were sterilized using ethylene oxide (EO) gas at the Suranaree University of Technology Hospital.

Table 1 the total designed experiment of composited material from design expert program.

Run	PLA (%)	PBS (%)	Nanocellulose (%)
1	77.50	17.50	5.00
2	65.00	26.71	8.29
3	77.50	17.50	5.00
4	65.00	26.71	8.29

Run	PLA (%)	PBS (%)	Nanocellulose (%)
5	90.00	7.11	2.89
6	76.30	23.70	0.00
7	90.00	7.11	2.89
8	84.10	11.53	4.37
9	77.50	17.50	5.00
10	65.00	35.00	0.00
11	82.62	7.38	10.00
12	74.69	15.31	10.00
13	82.53	17.47	0.00
14	88.58	1.42	10.00
15	70.14	28.99	0.87
16	77.50	17.50	5.00
17	82.53	17.47	0.00
18	69.24	20.76	10.00
19	88.58	1.42	10.00

hWJ-MSC isolation and culture

Human umbilical cords (n=2) were obtained from Maharat Nakhon Ratchasima Hospital (Nakhon Ratchasima, Thailand), for which informed consent was obtained from the mothers in accordance with the Ethics Committee for Research Involving Human Subjects of Suranaree University of Technology (EC-64-125). The cords were approximately 7 - 10 cm long and were washed with phosphate buffered saline (-) (PBS (-)). hWJ-MSCs were isolated from the umbilical cords and cultured as described previously [18]. Briefly, gelatinous Wharton's Jelly tissues were collected and sliced into small pieces (2 - 5 mm^2), placed in 90×15-mm culture dishes, and grown in the alpha modification of Eagle's medium (α-MEM) enriched with 2 mM L-glutamine, 100 U/mL penicillin, 100 µg/mL streptomycin, and 10 % fetal bovine serum (FBS). The MSCs were expanded until passage 3, cryopreserved with 10 % dimethyl sulfoxide (DMSO) in culture media, and then stored in liquid nitrogen.

Cell culture on scaffold

For cell seeding, approximately 1.0×10^5 hWJ-MSCs were plated on 4-well dishes (Nunc, Roskilde, Denmark), which had been precoated with 0.1 % gelatin. The cells were cultured in a complete medium (α-MEM supplemented with 10 % FBS). In the following hepatogenic differentiation protocol, the optimal scaffold was incorporated at the beginning of the process. Cells were first cultured in serum-free IMDM (Iscove's modified Dulbecco's medium) supplemented with 10 ng/mL bFGF (human basic fibroblast growth factor), 20 ng/mL EGF (epidermal growth factor), 100 µg/mL streptomycin, 100 U/mL penicillin, and 1 mM NaBu (sodium butyrate) for 3 days as a pretreatment. The cells were then induced to differentiate into the hepatic lineage using serum-free IMDM supplemented with 10 ng/mL bFGF, 40 ng/mL HGF (hepatocyte growth factor), and 5 mM nicotinamide for 7 days. Finally, the cells underwent a maturation step in serum-free IMDM supplemented with 10 ng/mL OSM, 10 nM dexamethasone, and 1 % ITS-X (insulin-transferrin-selenium-ethanolamine) for 7 days. The culture medium was changed twice weekly throughout the differentiation process [19].

Characterizations

Particle analysis and FTIR spectroscopy

For particle analysis, the average size, zeta potential, and polydispersity index of the nanocellulose samples were characterized using a Zetasizer Nano ZS instrument (Malvern, UK). For the FTIR analysis, nanocellulose powder was prepared using a diamond compression cell (S.T. Japan Europe, Germany), which

was equipped with 2 disks and a diamond window with a diameter of 3 mm. A thin layer of nanocellulose was added to the window using a needle, followed by compact closure with the 2 disks.

Synchrotron radiation-based FTIR spectroscopy was used to analyze chemical modifications in the nanocellulose. This technique uses a synchrotron infrared source and was performed at Beamline 4.1 of the Thai Synchrotron National Lab. This was operated in conjunction with a Bruker VEXTEX 70 vacuum FTIR spectroscopy system linked to a Bruker Hyperion 2000 IR microscope (Bruker Optics, Ettlingen, Germany). The microscope was equipped with a 36× objective and a mercury cadmium telluride detector that was cooled with liquid nitrogen.

The nanocellulose sample was measured in transmission mode using a spot size of 20×20 μm². Background subtraction was performed, and 64 scans were co-added with a spectral resolution of 4 cm^{-1}. The collected spectral data were analyzed using the software OPUS 7.5. Finally, principal component analysis (PCA) of the FTIR spectra was conducted in the wavenumber ranges of 3630 - 2770 and 1720 - 900 cm^{-1} by second-derivative analysis. This analysis used the Savitzky–Golay smoothing function within the software Unscrambler X version 10.4.

WAXS

WAXS experiments were performed at Beamline 1.3 W of the Synchrotron Light Research Institute (public organization), Thailand. The samples were exposed to X-rays with a wavelength of 0.137 nm for 600 s at room temperature. The sample-to-detector distance (SDD) was set to 167 mm. The raw data were preprocessed using the SAXSIT program developed by SLRI staff to generate a 1D WAXS curve. This curve was then analyzed using the pseudo-Voigt function within the SAXSIT software to determine the crystallinity index of the nanocellulose.

Thermal characterizations

The thermal stability of the samples was evaluated using thermogravimetric analysis (TGA) under an inert nitrogen atmosphere with a flow rate of 30 mL/min using a TGA instrument (TGA/DSC1, Mettler Toledo, USA). Approximately 2 mg of each sample was loaded onto a sample pan and heated from 30 to 500 °C at a constant heating rate of 10 °C/min. The onset temperature of weight loss and the temperature corresponding to the maximum degradation rate were determined.

The thermal properties of the samples were analyzed using differential scanning calorimetry (DSC) (DSC 204F1, NETZSCH, Germany) under a nitrogen atmosphere at a heating rate of 10 °C/min. The samples were heated from 20 to 250 °C, and the glass transition temperature (T_g), melting temperature (T_m), and melting enthalpy (H_m) were recorded. The degree of crystallinity (X_c) of PLA and PBS in the scaffold was then calculated from the melting enthalpy values according to the following equation:

$$X_c(\%) = \frac{\Delta H_m}{f_p \times \Delta H_m^\circ} \times 100\ \% \quad (1)$$

where ΔH_m (J/g) is the melting enthalpy of the polymer matrix measured by DSC, f_p is the weight fraction of PLA or PBS in the sample, and ΔH_m° (J/g) is the melting enthalpy of pure crystalline PLA (93 J/g) or PBS (200 J/g) [20].

Tensile force

Uniaxial tensile testing was performed at ambient temperature to characterize the mechanical properties of the scaffold samples. The analysis was performed using a TA. XT Plus SMS Stable Micro Systems Texture Analyzer (Stable Microsystems Ltd., Surrey, England) equipped with Texture Expert software. The scaffold specimens measured 0.1 mm in width, 50 mm in height, and 20 mm in length. The testing protocol involved subjecting the specimens to a controlled tensile load. The specific parameters for the test were as follows: pre-test speed of 1.0 mm/s, test speed of 1.5 mm/s, post-test speed of 10.0 mm/s, trigger type set to auto-5 g, and tare mode disabled.

Contact angle measurement and microscopy

The contact angles of the scaffold were analyzed using ultrapure water and cell culture medium. The analysis was performed using sessile drop method in the Agriculture and Bioplasma Technology Center, Thailand. Equilibrium contact angles (considered at 60 s) were measured for 5-μL droplet volumes. Determinations were made at 5 different locations for

each condition. The structural surface morphology of the nanocellulose samples and cell adhesion on the scaffold were investigated using field emission scanning electron microscopy (FESEM) (Zeiss, AURIGA, Germany) to assess surface features. Transmission electron microscopy (TEM) (FEI, Tecnai G2 20 TEM, USA) was used to image the nanocellulose at the Microscopy Laboratory of Suranaree University of Technology.

Cytotoxicity analysis

The cytotoxicity of the scaffolds was examined by replating 1000 hWJ-MSCs in 96-well culture plates (SPL Life Sciences, Gyeonggi-do, Korea) and culturing them in a culture medium for 24 h to allow attachment. The cytotoxicity of the optimal scaffold was evaluated by adding it to the culture medium. All cultures were maintained at 37 °C for 48 h in a humidified atmosphere with 5 % CO_2. The effects of the scaffold on cell viability were quantified using a 3-(4,5-dimethylthiazol-2-yl)-2,5-diphenyl tetrazolium bromide (MTT) assay. The absorbance was measured at 540 nm by a microplate reader (Varioskan LUX, Thermo Scientific, USA).

Immunofluorescence staining

Immunofluorescence staining was employed to evaluate protein expression profiles in cells undergoing a 17-day differentiation process on the scaffold. Cells were harvested on day 17 and fixed with 4 % PFA for 15 min. Blocking and permeabilization were then performed for 2 h at room temperature using a solution containing bovine serum albumin (BSA), normal goat serum, sodium azide, and Triton-X 100. The cells were then incubated overnight at 4 °C with primary antibodies targeting the specific proteins of interest: Anti-alpha-fetoprotein (AFP) antibody, anti-cytokeratin 18 (CK18) antibody, and anti-albumin (ALB) antibody. Following incubation, the cells were washed and then exposed to corresponding secondary antibodies for 2 h. Nuclei were visualized by staining with DAPI (4′,6-diamidino-2-phenylindole), and protein expression was observed using a fluorescence microscope.

Results and discussion

Morphological analysis of cellulose

Chemical analysis of the dried cellulose revealed a primary composition of cellulose fibers (**Figure 1(A)**) with a lignin content of 0.53 % and a hemicellulose content of 6.63 %. FESEM was employed to investigate the initial cellulose morphology, as presented in **Figure 1(E)**. The initial cellulose mixture had an average particle size of 43 μm before undergoing high-pressure homogenization and enzymatic processing. The homogenized mixture, the enzyme-treated product, and the nanocellulose powder are shown in **Figures 1(B)** - **1(D)**.

The morphology of cellulose processed solely through mechanical means is illustrated in **Figure 1(F)**. The image shows that there was extensive fibrillation, which is a consequence of high-pressure homogenization at 10,000 psi for 5 cycles. **Figure 1(G)** shows the nanocellulose obtained through the synergistic application of high-pressure homogenization and enzymatic hydrolysis. Notably, the nanocellulose exhibits a markedly reduced particle size compared to cellulose processed solely by mechanical techniques. The enzymatic hydrolysis was postulated to have instigated a cascade of complex reactions that ultimately transformed the cellulose fibril morphology into a more spherical configuration. **Figure 1(H)** shows a TEM image of the crystal structure of the nanocellulose derived from the combined methods.

(A)

(B)

(C)

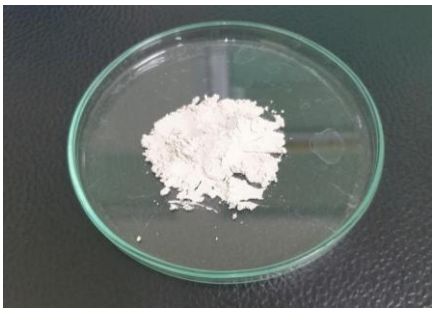

(D)

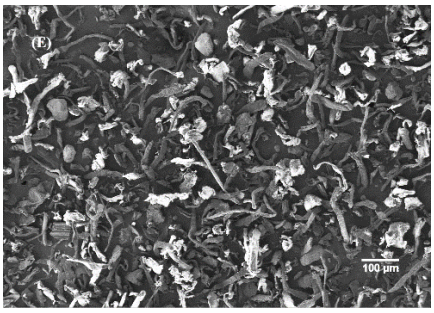

(E)

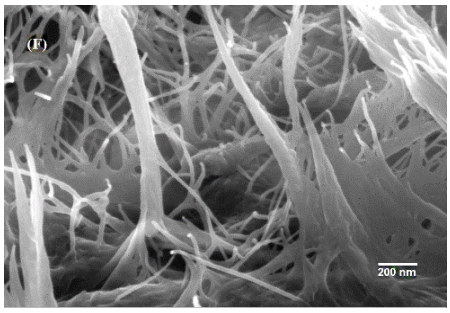

(F)

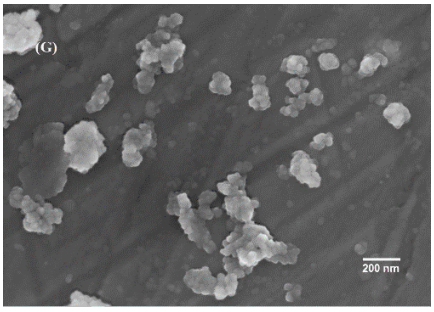

(G)

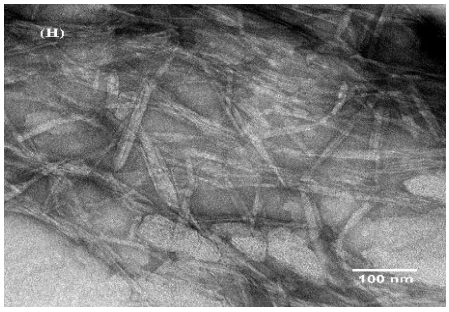

(H)

Figure 1 Image of sample in nanocellulose preparation (A) dried cellulose, (B) homogenized cellulose mixture, (C) enzyme-containing product (homogenized cellulose mixture was added by enzyme) and (D) nanocellulose powder, (E) FESEM image of sieved cellulose, (F) FESEM image of cellulose nanofibrils from high pressure homogenization at 10,000 psi 5 pass, (G) FESEM image of nanocellulose from high pressure homogenization at 30,000 psi, 15 pass couple with enzymatic process (7 % of enzyme), (H) TEM image cellulose nanocrystal from high pressure homogenization at 30,000 psi, 15 pass couple with enzymatic process (7 % of enzyme).

Particle analysis

Nanocellulose was analyzed to determine its average particle size (**Figure 2(A)**). Optimal particle size reduction of 278.9 nm was achieved using high-pressure homogenization at 30,000 psi for 15 passes with the addition of a 7 % enzyme cocktail. The findings suggest that the enzyme cocktail played a substantial role in facilitating size reduction, and high-pressure homogenization augmented this effect. The cellulose nanofibers (CNF) were examined in PBS for tissue engineering scaffolds and reported that CNFs with lengths of 500 - 800 nm and diameters below 50 nm resulted in the best combination of mechanical strength and cell attachment properties [21]. In addition, biocompatibility aspects of nanocellulose were studied in various polymers and found that for biomedical implants, CNFs with aspect ratios (length/diameter) between 70 - 100 showed reduced inflammatory responses while maintaining mechanical advantages [22]. The optimal size of nanocellulose for biomedical applications remains unclear. This is because nanocellulose size significantly influences the mechanical properties of the composite. However, the ideal size depends on the specific biomedical application and its intended purpose.

The zeta potential is a physicochemical property that quantifies the electrostatic potential at the interface between a solid particle and a surrounding liquid, and the results for the nanocellulose samples are presented in **Figure 2(B)**. Intriguingly, the zeta potential exhibited a significant reduction to approximately −20 mV after high-pressure homogenization at 30,000 psi for 15 cycles. This observation suggests a pressure-dependent decline in the potential during homogenization. The decrease could potentially be attributed to the exposure of anionic functional groups on the surface of the nanocellulose.

This phenomenon may result from cellulose fiber release or alterations of the surface chemistry induced by the mechanical stress of homogenization, as reported previously [23]. Conversely, the enzymatic treatment is not recognized to introduce negatively charged groups onto the surface of the nanocellulose. Notably, materials with lower negative zeta potential values are generally considered more favorable for specific biomedical applications [24].

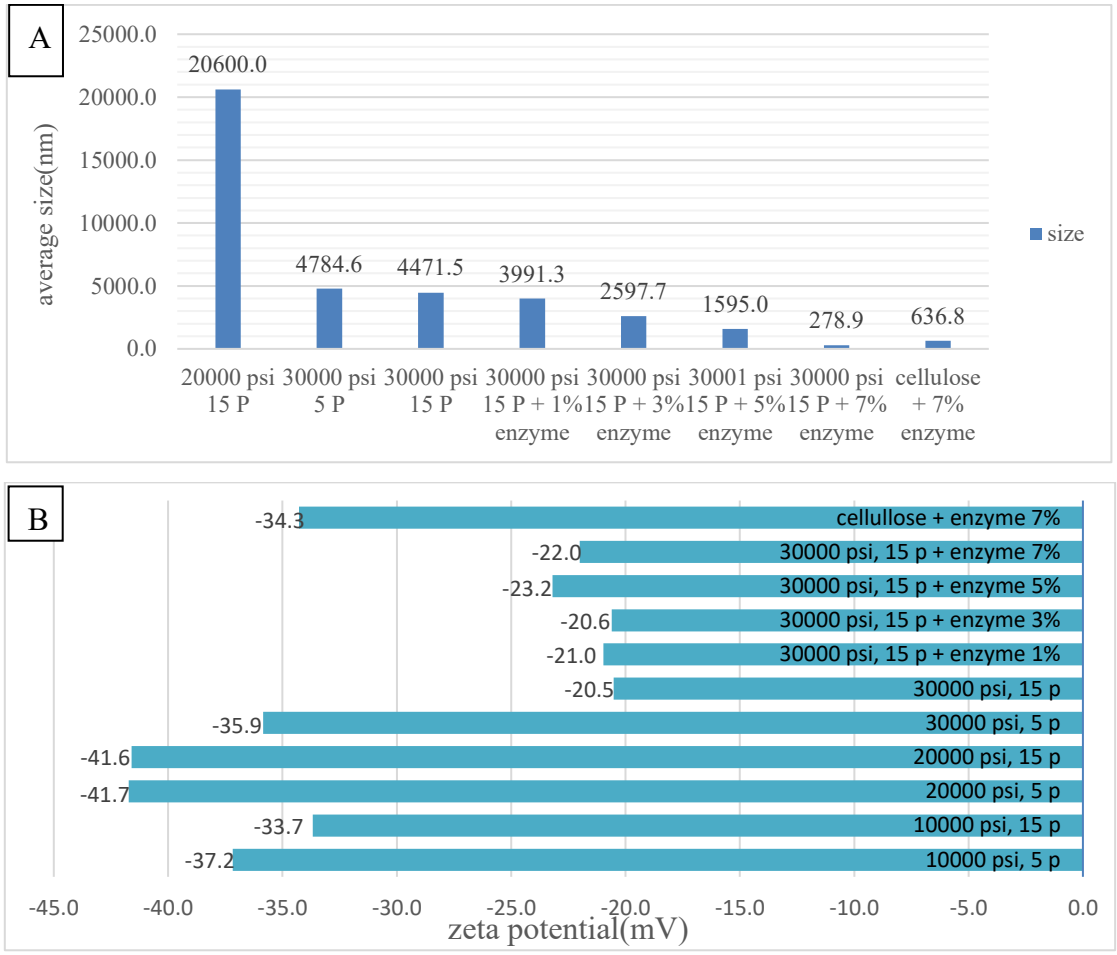

Figure 2 (A) average size (nm) of nanocellulose with different conditions, (B) zeta potential (mV) of nanocellulose with different conditions.

Polydispersity index of nanocellulose

The polydispersity index (PDI) was used as a metric to evaluate the distribution of particle sizes within the nanocellulose samples. **Table 2** shows the PDI values for nanocellulose produced under various processing conditions. The structural modifications induced by high-pressure homogenization were hypothesized to render the cellulose fibrils more amenable to enzymatic degradation during subsequent hydrolysis. This enhanced susceptibility to enzymatic hydrolysis can be attributed to the substantial shortening of the fibrils observed following enzymatic treatment. As a direct consequence, the incorporation of enzymes resulted in a significant elevation of the PDI of the nanocellulose. The enzyme cocktail functions synergistically, though each enzyme follows a distinct action pattern, further contributing to size heterogeneity. The increased PDI indicates a broader particle size distribution after enzymatic treatment. While the average particle size may decrease, the resulting population becomes more diverse, comprising both very small fragments from regions highly susceptible to enzymatic attack and larger fragments from more resistant regions.

Table 2 Polydispersity index (PDI) of nanocellulose with different conditions.

Sample	PDI
20000 psi 15 P	0.554
30000 psi 5 P	0.390
30000 psi 15 P	0.462

Sample	PDI
30000 psi 15 P + 1 % enzyme	0.567
30000 psi 15 P + 3 % enzyme	0.616
30001 psi 15 P + 5 % enzyme	0.669
30000 psi 15 P + 7 % enzyme	0.752
cellulose + 7 % enzyme	0.720

FTIR analysis

FTIR spectroscopy is a well-established analytical technique that was used to elucidate the chemical functionalities and structural characteristics of cellulose. Cellulose exists in 2 primary polymorphic forms: Cellulose I (native cellulose) and Cellulose II (regenerated cellulose). Cellulose I, found in nature, consists of parallel β-1,4-linked glucose chains and exists in 2 subtypes: Iα (triclinic) and Iβ (monoclinic). It is metastable, highly crystalline, and mechanically strong but difficult to dissolve. In contrast, Cellulose II, formed by mercerization or regeneration, has an antiparallel chain arrangement with stronger hydrogen bonding, making it thermodynamically stable, more soluble, and easier to process. While Cellulose I is the natural form, Cellulose II is preferred for industrial applications due to its enhanced solubility and processability [25-27]. The average spectra obtained for the nanocellulose are presented in **Figure 3(A)**. PCA was used to characterize the spectra. When applied to spectroscopic data, PCA typically yields 2 primary types of information. First, the expression of a group of similar spectra within the dataset was visualized in a scatter plot (**Figure 3(B)**). The 2D PCA score plot shows PC-1 (contributing 30 % of the variance) versus PC-2 (contributing 6 % of the variance). The FTIR spectral bands were summarized in **Table 3**.

Table 3 FTIR spectral bands and assignments.

Peak (cm^{-1})	Assignment	Reference
3490, 3442	Intramolecular OH (cellulose II)	[28,29]
3320	Intramolecular OH (cellulose)	[28,29]
3339	Intermolecular OH (cellulose Iα and Iβ)	[28,29]
3276	Intermolecular OH (cellulose Iβ)	[28,29]
2919	CH stretching vibration	[28,29]
2965	CH_2 asymmetric stretching (cellulose)	[28-30]
2852	CH_2 symmetric stretching (cellulose)	[28-30]
1511	Aromatic skeletal vibration (lignin)	[31,32]
1459, 1373, 1315	CH_2 bending vibration (crystalline cellulose I)	[29,30]
1425	CH_2 asymmetric stretching (amorphous cellulose)	[29,30]
1384	C-H (cellulose)	[28,29]
1278	CH deformation (cellulose I and II)	[29,30,32]
1174, 1128	C-O-C (cellulose)	[29,30]
1162, 1120	C-O-C asymmetric stretching (cellulose I and II)	[30,32,33]
1072, 1041, 1000	-C-O- (cellulose)	[29,30,32,33]
1062, 1029, 995	C-O vibration and C-O valence vibration (cellulose)	[34,35]

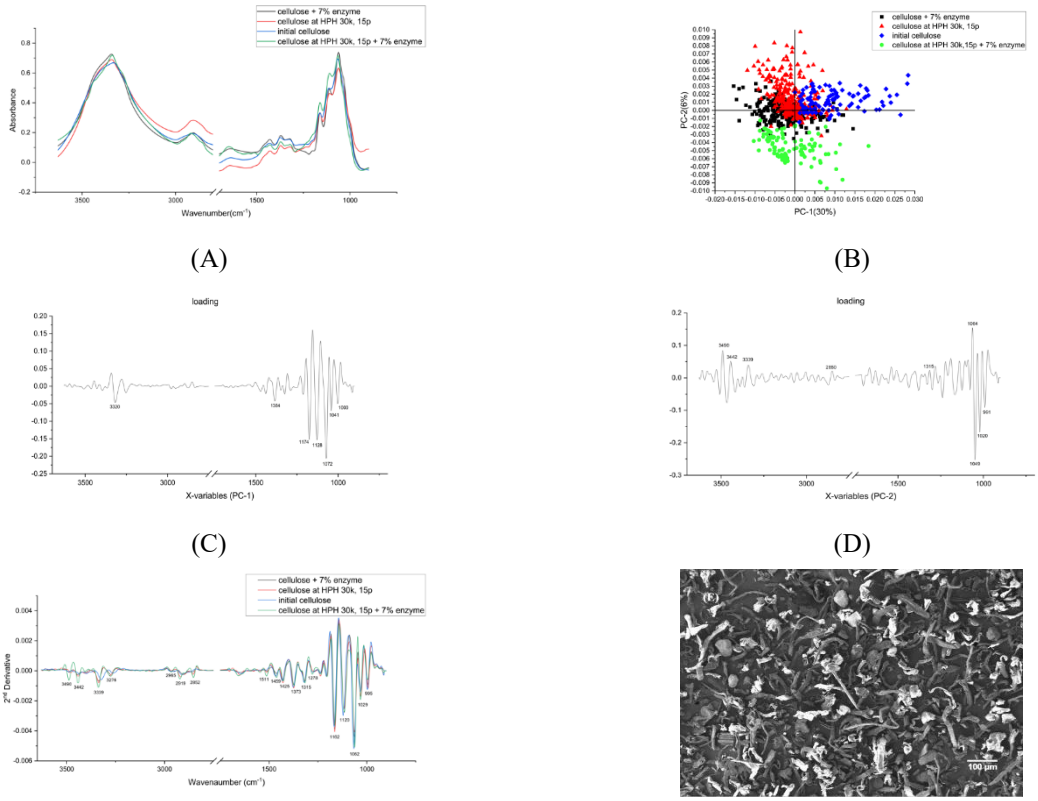

Figure 3 (A) The original average FTIR spectra of nanocellulose in different conditions and initial cellulose in wavenumber ranges of 3630 - 2770 and 1720 - 900 cm^{-1}. (B) The principal component analysis (PCA) score plot of FTIR spectra Principal component analysis score plots and (C) - (D) loading plots of PC-1 and PC-2, (E)The average second derivative spectra obtained from FTIR spectra nanocellulose in different conditions and initial cellulose. The spectra after 13 points of smoothing and normalized with extended multiplicative signal correction over the range of 3630 - 2770 and 1720 - 900 $cm^{-1}$from 2nd derivative spectra of nanocellulose in different conditions and initial cellulose. Spectra derived using second-derivative processing with the entire biochemical fingerprint region (1800 - 900 cm^{-1}) and (3500 - 2800 cm^{-1}).

The second type of information is the loadings that corresponded to the influence of specific spectral features on the observed variation, as shown in **Figures 3(C) - 3(D)**. The negative loading plot is illustrated in **Figure 3(C)**, which is related to the positive score plot of the initial cellulose by PC-2 (represented by the blue symbol). The negative loadings corresponding to the peaks at 3320 cm^{-1} (intramolecular OH cellulose), 1384 cm^{-1} (C-H in cellulose), 1174 and 1128 cm^{-1} (C-O-C in cellulose), 1072, 1041, and 1000 cm^{-1} (-C-O- in cellulose) indicate a strong association of these wavenumbers with the initial cellulose structure. Conversely, the positive loading plot (**Figure 3(D)**) was associated with the negative score plot of the cellulose processed with high-pressure homogenization at 30,000 psi for 15 cycles with the addition of 7 % enzyme (represented by the green symbol) by PC-2.

The positive loadings related to peaks at 3490 and 3442 cm^{-1} (intramolecular OH cellulose), 3339 cm^{-1} (intermolecular OH cellulose), 2850 and 1315 cm^{-1}(CH_2 in cellulose), and 1064 cm^{-1} (C-OH in cellulose) suggest a prominent contribution of these functionalities to the spectral variations observed in the cellulose treated with high-pressure homogenization and enzymes. Additionally, the negative loadings related to peaks at 1064, 1020, and 991 cm^{-1} (-C-O- in cellulose) imply potential structural modifications in these regions following the combined high-pressure homogenization and enzymatic treatment. The second derivative analysis of designated spectral regions within the FTIR spectra, as depicted in **Figure 3(E)**, the band around 3490 and

3442 cm^{-1} was employed to comparatively assess the nanocellulose samples processed under various conditions with the pristine cellulose.

The co-localized band observed at these wavenumbers corresponds to intramolecular hydrogen bonding within cellulose II [28,29], whereas the peak at 3339 cm^{-1} is characteristic of intramolecular hydrogen bonding in cellulose Iα and Iβ. The peak at 3276 cm^{-1} is attributed to intermolecular hydrogen bonding in cellulose Iβ. Both the mechanical processing and enzymatic hydrolysis treatments are known to augment the surface area of the cellulose particles, thereby exposing a greater number of hydroxyl (OH) groups. This phenomenon manifests as a more intense and well-defined peak at the OH stretching frequency within the FTIR spectra. The intensity of the intermolecular hydrogen bonding peak (3276 cm^{-1}) serves as an indicator of the crystallinity of cellulose. The observed enhancement in OH stretching intensity associated with intramolecular hydrogen bonding suggests a transformation of the crystalline structure towards a more amorphous state following the combined application of mechanical and enzymatic treatments.

The band at 2919 cm^{-1} corresponds to CH stretching vibration, while the bands at 2852 and 2965 cm^{-1} are assigned to CH_2 symmetric and asymmetric stretching vibrations in cellulose, respectively [29,30]. The band at 1511 cm^{-1} is attributed to aromatic skeletal vibration in lignin [31,32] and suggests the efficacy of both delignification methods in disrupting the lignin structure. The peaks at 1459, 1373, and 1315 cm^{-1} are associated with CH_2 bending vibration in crystalline cellulose I, while the peak at 1425 cm^{-1} corresponds to CH_2 asymmetric stretching vibration in amorphous cellulose [29,30]. The peak at 1278 cm^{-1} is attributed to CH deformation in both cellulose I and II, the C-H deformation at 1278 cm^{-1} may be influenced by the enzymatic hydrolysis of glycosidic bonds in cellulose. [29,30,32]. The peaks at 1162 and 1120 cm^{-1} are indicative of C-O-C asymmetric stretching vibration in cellulose I and II [30,32,33]. Finally, the peaks at 1062, 1029, and 995 cm^{-1} are assigned to C-O vibration and C-O valence vibration in cellulose [34,35].

High-pressure homogenization alters the chemical architecture of cellulose by fragmenting the fibers into nanoscale particles. This process disrupts existing hydrogen bonds within the cellulose fibers and potentially facilitates the formation of new ones. The high pressure and shear forces can also induce mechanical stress, which promote the formation of new hydrogen bonds between cellulose molecules and result in a more densely packed and organized structure [36]. Enzymatic hydrolysis modifies the chemical structure by generating new chemical functionalities on the surface of the cellulose fibers as it cleaves the glycosidic bonds [37]. These modifications can further influence the chemical composition of the resulting nanocellulose [38].

Crystallinity analysis

WAXS analysis is a well-established technique for characterizing crystalline structures. The WAXS patterns of the nanocellulose samples are presented in **Figure 4(A)**. The characteristic scattering peaks for cellulose I were observed at 2θ = 14.8, 16.3, 20.6, 22.4, and 34.4 ° [39], while those for cellulose II were identified at 2θ = 12.4, 20.2, and 21.8 ° [39]. The peaks at 2θ = 26.5 and 27.8 ° were attributed to natural graphite [40] and natural silver chloride Cheng *et al.* [39], respectively. The unidentified peaks at 2θ = 36.4 and 39.2 ° could potentially originate from natural minerals present in the sample.

The crystallinity index (CI) of cellulose was determined using the WAXS deconvolution method implemented in SAXSIT software. This method involves separating the amorphous and crystalline contributions in the WAXS spectrum through curve fitting using Voigt functions. The resulting CI values are shown in **Figure 4(B)**. The initial cellulose exhibited a high CI of 59.2 %, but high-pressure homogenization led to a decrease in CI, possibly due to the disruption of the crystalline structure by the high-pressure forces. Conversely, enzymatic hydrolysis initially resulted in an increase in CI with increasing enzyme concentration up to 5 %. However, CI decreased to 50 % when 7 % enzyme was added.

During homogenization, the mechanical forces can disrupt hydrogen bonding networks within cellulose crystalline domains [41], the high shear forces and localized pressure differences randomly create structural defects in the crystalline regions, converting portions of crystalline cellulose to amorphous regions, and amorphous regions were destroyed, leading to the breakdown of the structure and size reduction.

For the enzymatic hydrolysis, the cellulase enzymes initially access and hydrolyze the more accessible amorphous regions [42,43]. The selective enzymatic hydrolysis preferentially attacks amorphous regions while leaving crystalline domains intact [44]. This selective degradation effectively increases the proportion of crystalline material in the remaining cellulose. In another hand, higher enzyme loadings or extended reaction times, enzymes begin attacking the crystalline domains after depleting most accessible amorphous regions [45]. Excessive enzymatic treatment can penetrate the ordered crystalline structure, creating defects and reducing overall crystallinity [46,47].

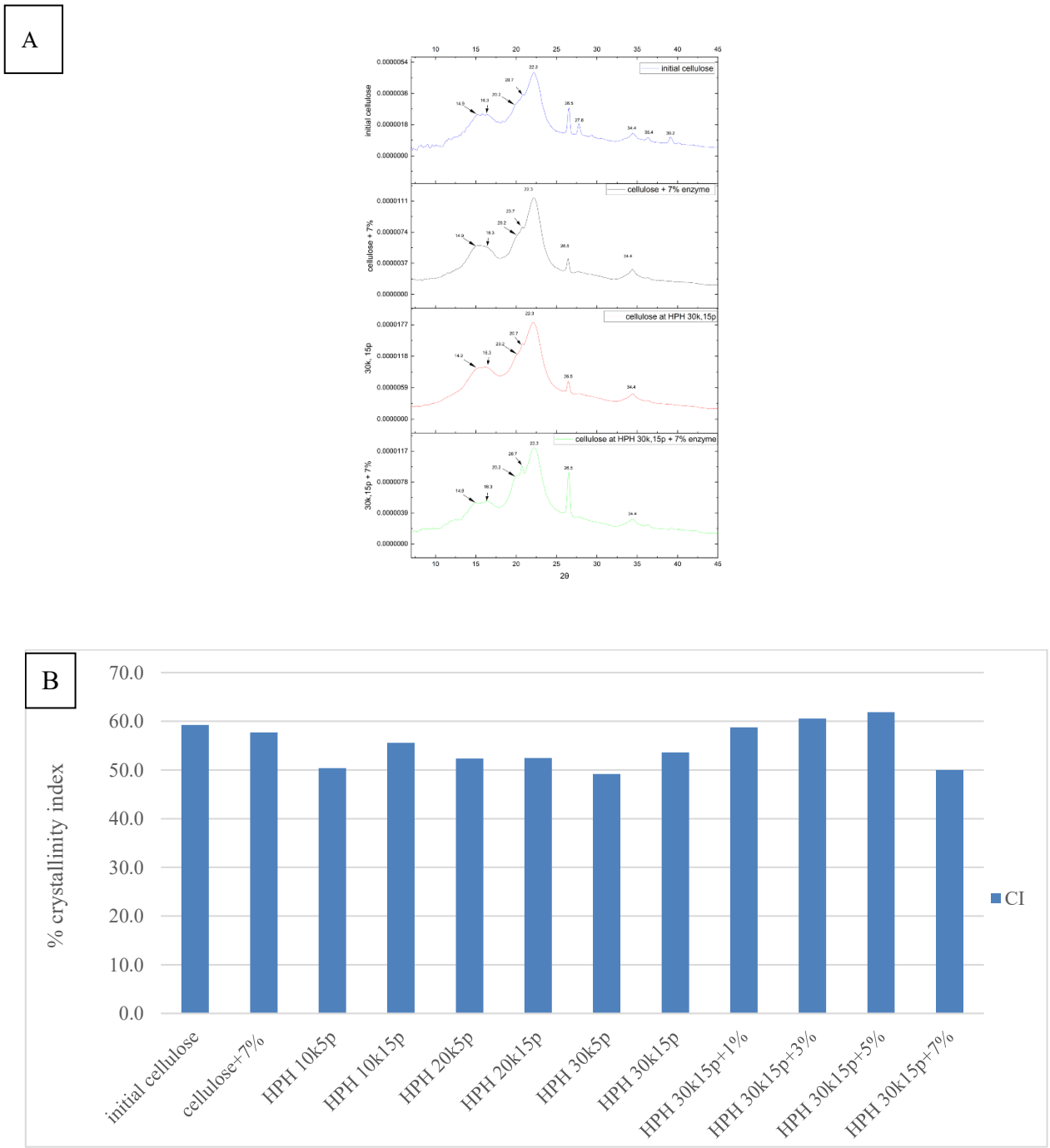

Figure 4 (A)WAXS patterns of nanocellulose in different methods compared with initial cellulose. (B) crystallinity index of cellulose in different methods.

Optimal scaffold production

High hydrophilicity and absorption are important properties for the design of cell culture scaffolds. These characteristics were evaluated by measuring the contact angles of water and cell culture media on the scaffolds. Additionally, the maximum tensile force was analyzed. Experiments were conducted according to the design outlined in **Table 4** with a total of 19 runs. The table shows the water contact angle, cell-culture-and medium contact angle, and maximum tensile force for each run. An analysis of variance (ANOVA) and response surface methodology (RSM) were used to analyze the influence of factors and the relationships between variables. Statistical values including the sequential model sum of squares, adjusted coefficient of determination, predicted coefficient of determination, and lack of fit were assessed to determine the suitability of the model.

Table 4 mixture designed experiment and results of water contact angle, medium contact angle and maximum tensile force.

Run	PLA(%)	PBS(%)	nanocellulose (%)	water contact angle(radius)	medium contact angle(radius)	average maximum tensile force(g)
1	77.50	17.50	5.00	73.29	79.76	1175.40
2	65.00	26.71	8.29	62.20	67.85	956.83
3	77.50	17.50	5.00	71.42	66.10	1175.40
4	65.00	26.71	8.29	64.36	61.43	956.83
5	90.00	7.11	2.89	60.79	60.69	1739.58
6	76.30	23.70	0.00	89.07	79.04	1344.92
7	90.00	7.11	2.89	69.87	62.17	1739.58
8	84.10	11.53	4.37	91.87	82.20	1649.75
9	77.50	17.50	5.00	73.86	73.44	1175.40
10	65.00	35.00	0.00	59.57	63.44	1456.92
11	82.62	7.38	10.00	82.21	74.42	1890.25
12	74.69	15.31	10.00	72.49	82.47	1203.28
13	82.53	17.47	0.00	83.12	82.37	1030.75
14	88.58	1.42	10.00	77.34	76.78	1640.72
15	70.14	28.99	0.87	72.60	62.43	1089.45
16	77.50	17.50	5.00	74.05	82.76	1175.40
17	82.53	17.47	0.00	98.34	113.72	1030.75
18	69.24	20.76	10.00	97.78	72.33	1330.40
19	88.58	1.42	10.00	77.23	76.38	1640.72

Statistical analysis was used to select a model equation that effectively describes the relationship between the water contact angle, maximum tensile force, and the composite material ratio of the cell culture scaffold. A quartic model exhibited the best fit for this relationship, but a quadratic model was more appropriate for the contact angle of the cell culture medium and the ratio. The suitability of the model equations for explaining or predicting experimental outcomes was evaluated using several coefficients, as shown in **Table 5**. These coefficients included the coefficient of determination (R^2), adjusted coefficient of determination (adj-R^2), predicted coefficient of determination (pred-R^2), and lack of fit (p-value).

Table 5 the data from ANOVA for fitted model.

Properties	Fitted model	Sequential *p*-value	*p*-value Lack of fit	R^2	adj-R^2	pred-R^2	C.V. (%)
water contact angle	special quartic quadratic	0.0046	0.2203	0.8772	0.779	0.2189	7.12
medium contact angle	quadratic linear	0.0347	0.432	0.5153	0.3288	0.0455	13.55
maximum tensile force	special quartic quadratic	0.0011	-	0.9203	0.8566	0.3237	8.41

The R^2 values for the water contact angle and maximum tensile force experiments were high (0.8772 and 0.9203, respectively). Generally, a higher R^2 value approaching unity indicates a stronger correlation between the model and the experimental data. In these instances, close agreement between the model predictions and the experimental observations suggests that the model equations can be used for accurate explanation or prediction.

However, the R^2 value for the cell culture medium contact angle experiment was lower (0.5153), which signifies a poor fit. This translates to a substantial discrepancy between the model predictions and the experimental results and low model accuracy for explanation and prediction in this context. For a robust model, the adj-R^2 value should be close to the R^2 value, and a high pred-R^2 value indicates efficacy of the model in predicting response values for novel data points. However, all 3 experiments exhibited relatively low pred-R^2 values, which suggest that the models are not well suited for predicting the response of new data.

The coefficient of variation (CV %) was examined through the ANOVA. A lower CV % value signifies less variance in the data relative to the mean. The CV % values for the water contact angle and maximum tensile force experiments were relatively low (7.12 and 8.41 %, respectively), which indicate minimal data variation. Conversely, the contact angle experiment with cell culture medium exhibited a higher CV %, which suggests greater data variance.

A statistically significant *p*-value for lack of fit indicates that the model inadequately describes the data. The *p*-values for lack of fit for the contact angle experiments with water and cell culture medium were 0.2203 and 0.4320, respectively, which suggest that the lack of fit is not statistically significant in these cases. However, the *p*-value for lack of fit in the maximum tensile force experiment was not reported. It is essential to assess this value to definitively determine the model's suitability for this relationship.

Finally, the Water contact angle, The model fits well with a high R^2 and reasonable C.V. The predicted R^2 is low, indicating potential issues in generalizing to new data. Medium contact angle, the model shows moderate fit, but the predicted R^2 is very low, suggesting the model may not generalize well to new data. Maximum Tensile force, the model shows an excellent fit with high R^2 and relatively low C.V., but the low predicted R^2 suggests caution in generalizing the model.

Assessment of a model's suitability for variance prediction necessitates residual plot analysis to support the predictions generated by the model equations. Commonly used plots for this purpose include normal probability plots of residuals, residuals versus predicted values, and predicted versus actual values. The residual plots for the water contact angle experiment are shown in **Figure 5**. The data points in the normal probability plot (**Figure 5(A)** (left)) exhibit a tight distribution around the regression line (red line), which signifies minimal deviations from the mean.

Similarly, the residuals in the residual versus predicted plot (**Figure 5(A)** (middle)) cluster around the zero line (black line) with no observations exceeding the control lines (red lines). This indicates a favorable distribution of data devoid of outliers. Finally, the plot of predicted versus actual values (**Figure 5(A)** (right)) demonstrates that the data points concentrate around the diagonal line (black line), which suggest low errors relative to the predicted values. Based on this residual

analysis, the model appears well suited for predicting the water contact angle.

However, the residual plots for the cell culture medium contact angle (**Figure 5(B)**) and maximum tensile force (**Figure 5(C)**) experiments reveal some limitations. In the normal probability plots (**Figures 5(B)** - **5(C)** (left)), certain data points (circled) deviate considerably from the regression line, which indicates substantial deviations from the mean. Furthermore, while most data points in the residual versus predicted plots (**Figures 5(B)** - **5(C)** (middle)) cluster near the zero line, a solitary circled data point falls outside the control lines, which suggests the presence of an outlier. Although most data points in the predicted versus actual plots (**Figures 5(B)** - **5(C)** (right)) lie close to the diagonal line, the circled data points exhibit significant errors compared to the predicted values.

These observations from the residual plots for the contact angle of the cell culture medium and the maximum tensile force suggest potential shortcomings in the model's capacity to predict these outcomes. While the elimination of outlying data points might seem appealing, a critical investigation into the underlying causes of these deviations is paramount. Re-analyzing the data after addressing these issues might enhance the model's predictive capability.

RSM is a statistical approach for optimizing production processes by generating a mathematical model that elucidates the interactions between various experimental variables. RSM can be used to visually represent the relationships between variables through contour plots. **Figure 5(D)** shows an example of this concept. Red areas in the plot show the highest observed values, yellow and green areas represent intermediate values, and blue areas show the lowest values.

In the contact angle experiment with water, as shown in **Figure 5(D)** (left), the red area is within the region of high PLA concentration. This observation implies that PLA addition leads to an increase in the water contact angle of the scaffold, which translates to a reduction in material hydrophilicity. Conversely, the incorporation of PBS and nanocellulose appears to enhance the hydrophilicity of the material. The contact angle experiment with cell culture medium (**Figure 5(D)** (middle)) exhibits analogous trends to those observed in the experiments with water. In this case, the maximum tensile force (**Figure 5(D)** (right)) demonstrates an increase with the addition of both PLA and nanocellulose, but it exhibits a decrease with the addition of PBS.

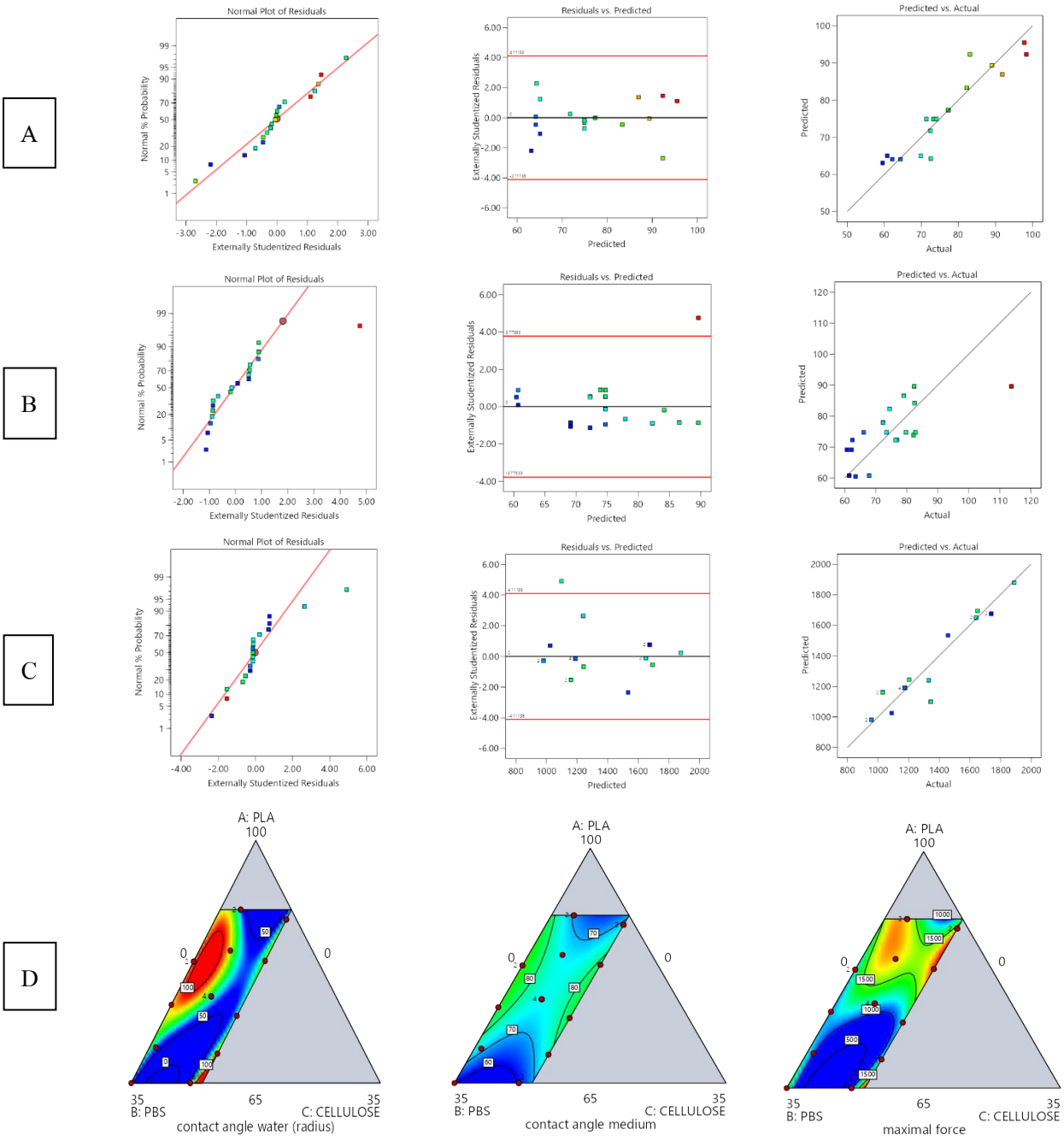

Figure 5 (A) verification of the model of the water contact angle experiment: Normal plot of Residual(left), Residual Vs. Predicted (middle), Predicted Vs. Actual (right), (B) verification of the model of the cell culture medium contact angle experiment: Normal plot of Residual(left), Residual Vs. Predicted (middle), Predicted Vs. Actual (right), (C) verification of the model of the maximum tensile force experiment: Normal plot of Residual (left), Residual Vs. Predicted (middle), Predicted Vs. Actual (right), (D) contour plot obtained after optimization (RSM): Contact angle of water (left), contact angle of cell culture medium (middle) and maximum tensile force (right).

RSM was used to optimize the ratio of composite materials under the following constraints: PLA content of 65 to 90 % (65 % ≤ PLA ≤ 90 %), PBS content ≤ 35 %, nanocellulose content ≤ 10 %, maximum combined PBS and nanocellulose content of 40 % (PBS + nanocellulose ≤ 40 %), and total content of 100 % (PLA + PBS + nanocellulose = 100 %). RSM analysis revealed that the optimal composition was 65.00 % PLA, 26.81 % PBS, and 8.19 % nanocellulose. This composition was validated through the fabrication of cell culture

scaffolds, which were characterized in terms of the contact angles for water and cell culture medium, as well as the maximum tensile force. As shown in **Figure 6**, the contact angles for water and cell culture medium under the optimal conditions were 67.72 and 65.61 °, respectively, and the maximum tensile force was measured as 651.425 g.

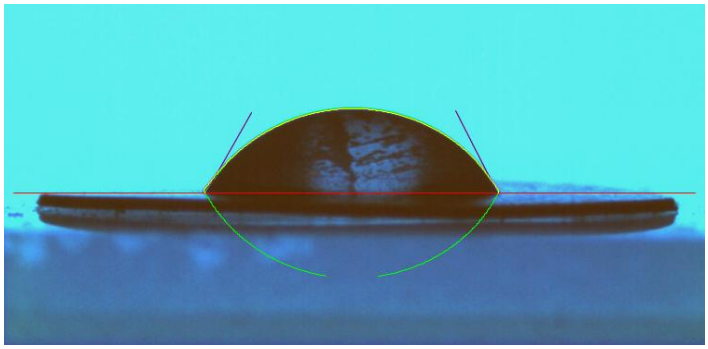

Contact angle of cell culture medium of 65.61 °

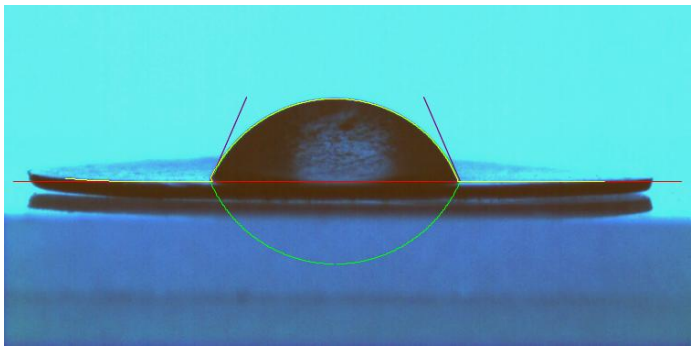

Contact angle of water of 67.72 °

Figure 6 contact angle images of cell culture medium (upper) and water (bottom).

Thermal stability and thermal property analysis

TGA was used to investigate the thermal degradation profiles of nanocellulose, PLA, PBS, PLA/PBS, and the composite scaffold, as illustrated in **Figure 7(A)**. The TGA results for nanocellulose exhibited a 2-stage weight-loss pattern. The initial stage occurred at approximately 180 °C and is likely attributable to the decomposition of inherent natural components. Notably, the final decomposition temperature of nanocellulose yielded the highest residual weight (29.64 %) compared to the other materials. In contrast, the residual weights of PLA, PBS, PLA/PBS, and the scaffold were 10.67, 6.26, 1.59, and 1.57 %, respectively. Nanocellulose retains the highest residual weight (29.64 %), indicating superior thermal stability due to its crystalline structure and the formation of carbonaceous residues that resist further degradation. In contrast, PLA (10.67 %) and PBS (6.26 %) decompose more extensively, with PBS exhibiting lower thermal stability than PLA. The PLA/PBS blend (1.59 %) and the scaffold (1.57 %) show the lowest residual weights, This suggests potential interactions between materials in the blend that may reduce overall thermal stability. The high biodegradability of PLA/PBS and the scaffold is advantageous for biomedical applications such as tissue engineering, where controlled degradation supports tissue regeneration.

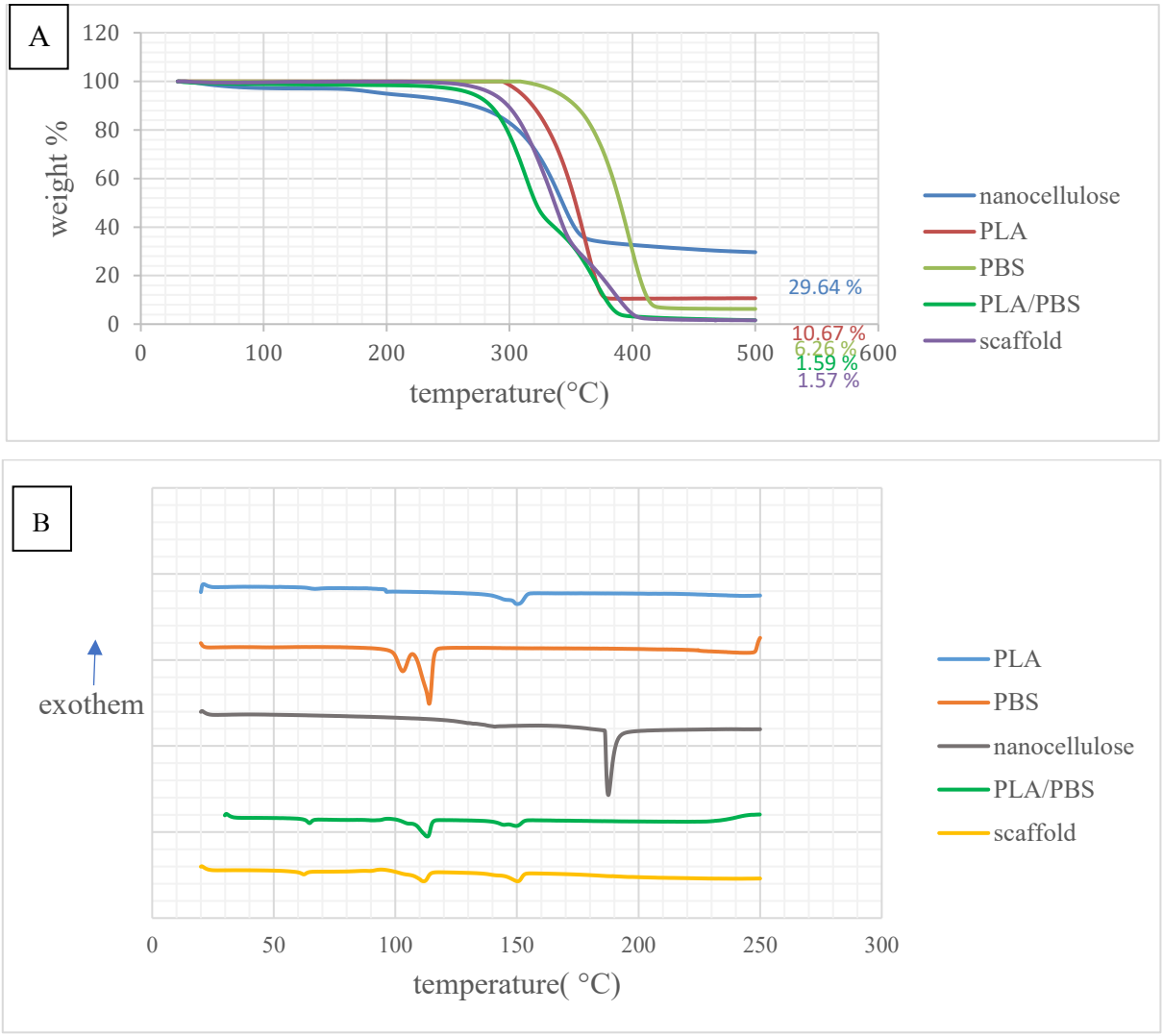

Figure 7 (A) weight loss of nanocellulose, PLA, PBS and scaffold (PLA 65.00 %, PBS 26.81 %, nanocellulose 8.19 %) at temperature of 20 to 500 °C, (B) DSC results of nanocellulose, PLA, PBS PLA/PBS (PLA 60 %, PBS 40 %) and scaffold (PLA 65.00 %, PBS 26.81 %, nanocellulose 8.19 %).

Table 6 TGA results of nanocellulose, PLA, PBS and scaffold (PLA 65.00 %, PBS 26.81 %, nanocellulose 8.19 %).

Sample	Starting decomposition temperature	Maximum decomposition temperature	Ending decomposition temperature
nanocellulose	290	340	381
PLA	297	359	390
PBS	320	376	427
PLA/PBS	260	311	409
Scaffold	260	334	415

Table 6 summarizes the critical parameters associated with thermal stability, including the onset decomposition temperature, the peak decomposition temperature, and the final decomposition temperature. It is noteworthy that the thermal degradation temperature of the scaffold exhibited a decrease relative to the individual components. This observation suggests that the blending process might have induced a chemical restructuring within the composite materials.

Table 7 DSC results of nanocellulose, PLA, PBS, PLA/PBS (PLA 60.00 %, PBS 40.00 %) and scaffold (PLA 65.00 %, PBS 26.81 %, nanocellulose 8.19 %).

Samples	PLA fraction				PBS fraction			
	T_g(°C)	T_m(°C)	H_m (J/g)	X_c(%)	T_g(°C)	T_m(°C)	H_m (J/g)	X_c(%)
PLA	67.1	150.4	31.88	34.27	-	-	-	-
PBS	-	-	-	-	-	113.9	129.3	64.65
PLA/PBS	64.7	149.5	16.23	29.09	-	113.9	37.45	46.81
Scaffold	62.3	150.4	19.87	32.87	-	111.7	27.04	50.41

DSC analysis was used to investigate the thermal properties of PLA, PBS, nanocellulose, and the composite scaffold. The findings are shown in **Figure 7(B)** and **Table 7** and provide valuable insights into the material behavior of the scaffold. The DSC thermogram of the nanocellulose revealed a distinct endothermic peak at 187.6 °C, which is attributable to the evaporation of inherent moisture content.

Interestingly, the glass transition temperature (T_g) and melting temperature (T_m) of the PLA fraction exhibited a slight reduction within both the PLA/PBS blend and the composite scaffold compared to pure PLA. The PLA/PBS blend displayed a T_g peak at approximately 64.7 °C and a T_m peak at 149.5 °C. The scaffold exhibited a T_g peak of around 62.3 °C and a T_m peak of 150.4 °C. Notably, the PBS fraction within both the blend and the scaffold displayed distinct T_m peaks at 113.9 and 111.7 °C, respectively. The crystallinity of both the PLA and PBS fractions within the scaffold also showed enhancement with the incorporation of nanocellulose, which suggests that nanocellulose may facilitate the rearrangement of ordered PLA and PBS molecular chains during the blending process. In this context, nanocellulose can be considered analogous to a nucleating agent that promotes the crystallization process within the composite scaffold.

Morphological analysis of scaffold

FESEM was used to investigate the morphological features of the surface of the nanocellulose-based biopolymer scaffold (composed of 65.00 wt% PLA, 26.81 wt% PBS, and 8.19 wt% nanocellulose). The FESEM image in **Figure 8** shows that the surface topography is characterized by abundant miniature pores and a striated texture. The cross-sectional area was also examined to provide further insights into the internal structure of the scaffold. The presence of these pores suggests that the scaffold possesses a porous microstructure, which is a crucial characteristic for applications in tissue engineering, as it facilitates cell adhesion, proliferation, and nutrient transport [48]. The striated texture observed on the surface may be attributed to phase separation between PLA and PBS, as these polymers have different miscibility and crystallization behaviors [49]. The incorporation of nanocellulose likely influences surface morphology by acting as a nucleating agent, leading to the formation of a more structured and interconnected network.

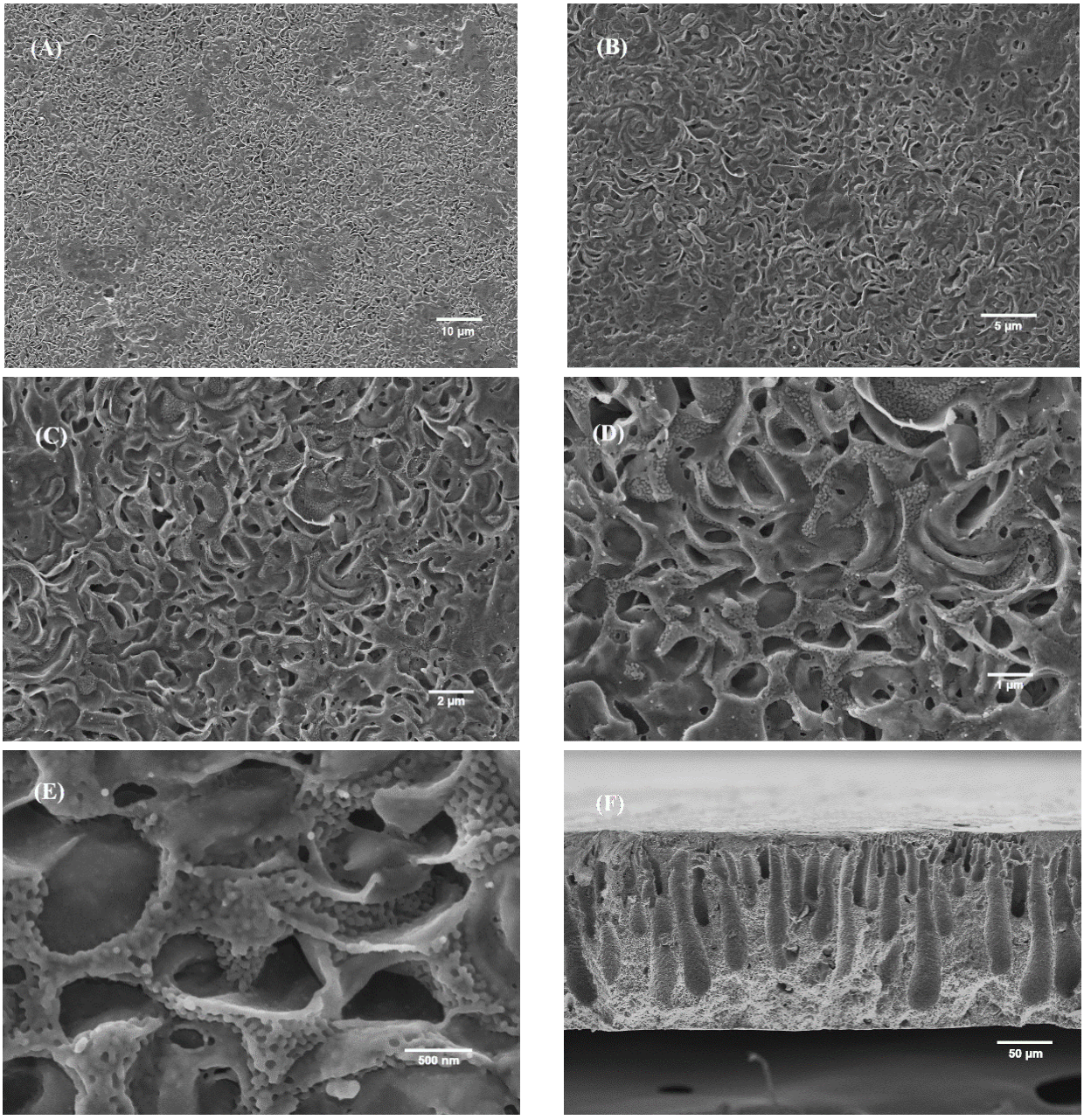

Figure 8 morphology of surface structure of nanocellulose based biopolymer scaffold (65.00% of PLA, 26.81% of PBS and 8.19% of nanocellulose) under FESEM : (A) scale bar of 10 µm, (B) scale bar of 5 µm, (C) scale bar of 2 µm, (D) scale bar of 1 µm, (E) scale bar of 500 nm, and (F) cross-sectional area of scaffold, scale of 50 µm.

hWJ-MSC viability on scaffold

An *in vitro* cytotoxicity evaluation of the scaffold was conducted. hWJ-MSCs were co-cultured with the scaffold material in complete medium for 72 h. Cell viability was then quantitatively assessed using the MTT assay. The experiment was performed in triplicate to ensure data reproducibility. The analysis revealed an average cell viability of 96.65 %.

Hepatogenic differentiation of hWJ-MSCs

The process of hepatogenic differentiation of hWJ-MSCs was evaluated microscopically on days 3, 6, 8, 10, 13, 15, and 17, as shown in **Figure 9**. Light microscopy observations revealed morphological alterations indicative of hWJ-MSCs transitioning towards a hepatocyte-like morphology. Specifically, no substantial changes in cellular morphology were observed on days 3 and 6. However, on day 8, the cells began to exhibit shape transformations, which

progressively continued towards the acquisition of a polygonal morphology by day 17. The timeline of morphological changes serves as a key indicator for validating the effectiveness of the differentiation protocol. The observed changes confirm the successful hepatogenic differentiation of hWJ-MSCs, allowing for the subsequent culture on the scaffold.

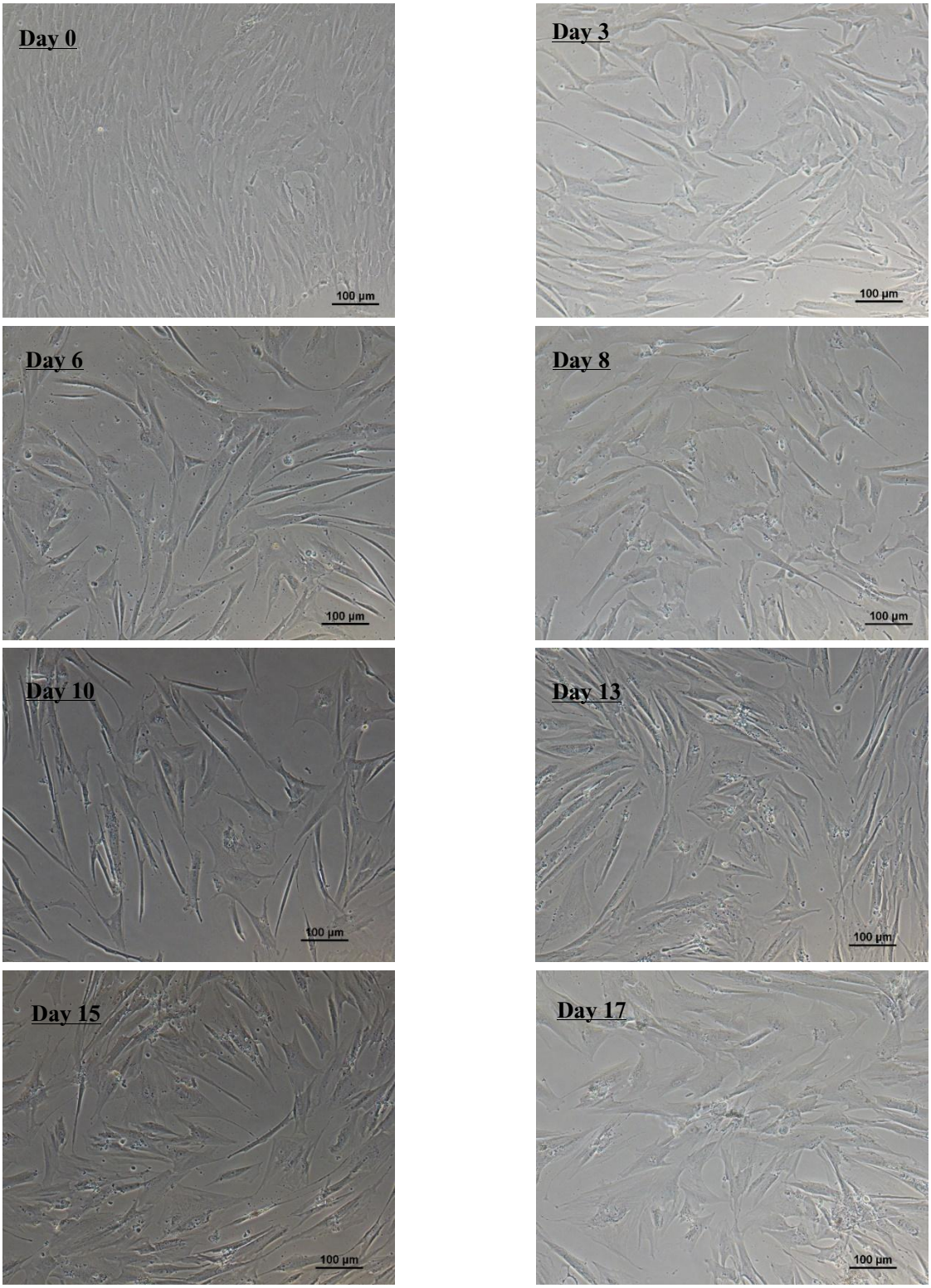

Figure 9 morphological change of Hepatogenic differentiation of Human Wharton's jelly – derived mesenchymal stem cells(hWJ-MSCs) for 17 days, scale bar of 100 µm.

Hepatogenic differentiation of hWJ-MSCs on scaffold and immunofluorescence staining

hWJ-MSCs were seeded onto the scaffold as shown in **Figure 10** (left) to promote their differentiation towards a hepatocyte lineage. The findings are shown in **Figure 10** (bottom) and support the successful differentiation of hWJ-MSCs into hepatocyte-like cells on the scaffold (65.00 wt% PLA, 26.81 wt% PBS, and 8.19 wt% nanocellulose). The expression of hepatic markers (AFP, CK18, and ALB) in hepatogenic differentiated cells was also investigated. Immunocytochemical analysis of the differentiated hWJ-MSCs on the scaffold revealed the presence of all 3 hepatic markers. This finding supports their successful differentiation towards a hepatocyte-like phenotype on the scaffold, as shown in **Figure 11**.

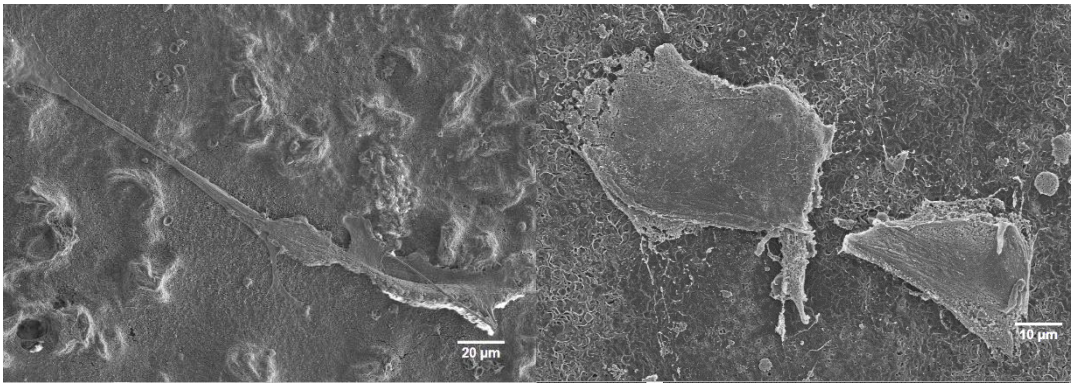

Figure 10 FESEM image of Human Wharton's jelly – derived mesenchymal stem cells (hWJ-MSCs) on nanocellulose based biopolymer scaffold (left) and FESEM image of hepatocyte on nanocellulose based biopolymer scaffold (right), Human Wharton's jelly – derived mesenchymal stem cells (hWJ-MSCs) were induced into hepatocyte on scaffold using modified protocol for 17 days.

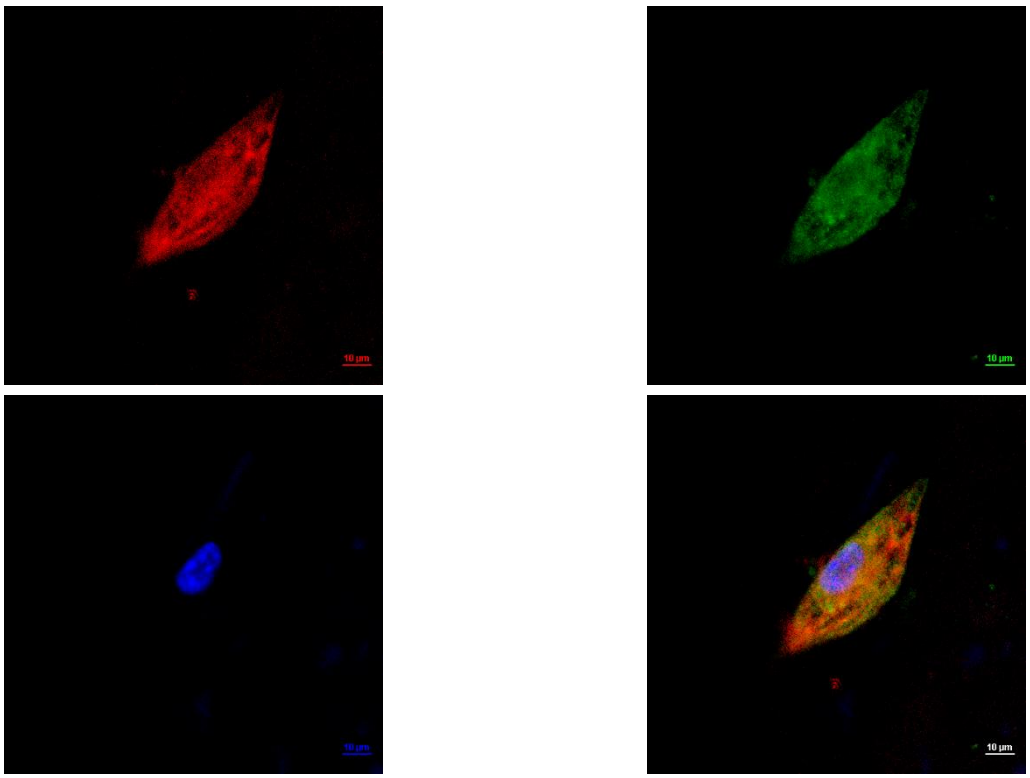

Figure 11 immunofluorescence analysis of hepatocyte on nanocellulose based biopolymer scaffold for 17 days., AFP, CK18 = red, ALB = green and DAPI = blue; nucleus, scale bar = 10 µm.

Conclusions

Nanocellulose was fabricated using a synergistic approach that combines high-pressure homogenization and enzymatic digestion, resulting in the smallest nanocellulose with an average size of 278.9 nm. The optimal scaffold composition consisted of 65.00 wt% PLA, 26.81 wt% PBS, and 8.19 wt% nanocellulose, exhibiting good hydrophilic properties. Biopolymer scaffolds incorporating nanocellulose demonstrate significant potential for tissue engineering applications due to their biocompatibility and safety profile. The scaffold showed the lowest residual weight (1.57 %), suggesting a high degree of biodegradability, which is advantageous for controlled degradation in biomedical applications. Additionally, Cells exhibit strong adhesion at multiple sites on the scaffold and demonstrate effective hepatogenic differentiation. This study represents the initial phase in the development of scaffolds that could encourage enhanced cellular adhesion and lay the foundation for advancements in the field of tissue engineering.

Future *in vivo* studies will be essential to validate these promising *in vitro* results and thoroughly evaluate the scaffold's performance within a living organism, ultimately paving the way for potential clinical translation. However, this study has some limitations, particularly concerning the translation of these 2D findings into complex 3D structures, which are often required for functional tissue regeneration. The next steps in scaffold refinement involve not only optimizing the scaffold's mechanical properties and degradation rate but also focusing on the fabrication of 3D scaffolds with controlled architecture and porosity, potentially using techniques like 3D bioprinting, to better mimic the native tissue environment and enhance tissue formation.

Acknowledgements

This work was supported by (i) Suranaree University of Technology (SUT), Thailand, (ii) Thailand Science Research and Innovation (TSRI), Thailand, and (iii) National Science, Research and Innovation Fund (NSRF) (NRIIS number 179319).

References

[1] H Devarbhavi, SK Asrani, JP Arab, YA Nartey, E Pose and PS Kamath. Global burden of liver disease: 2023 update. *Journal of Hepatology* 2023; **79(2)**, 516-537.

[2] ML Dias, BA Paranhos and R Goldenberg. Liver scaffolds obtained by decellularization: A transplant perspective in liver bioengineering. *Journal of Tissue Engineering* 2022; **13**, 20417314221105305.

[3] S Castaneda-Rodriguez, M Gonzalez-Torres, RM Ribas-Aparicio, MLD Prado-Audelo, G Leyva-Gomez, ES Gurer and J Sharifi-Rad. Recent advances in modified poly (lactic acid) as tissue engineering materials. *Journal of Biological Engineering* 2023; **17(1)**, 21.

[4] L Aliotta, M Seggiani, A Lazzeri, V Gigante and P Cinelli. A Brief review of poly (butylene succinate) (PBS) and its main copolymers: Synthesis, blends, composites, biodegradability, and applications. *Polymers* 2022; **14(4)**, 844.

[5] F Luzi, E Fortunati, A Jimenez, D Puglia, D Pezzolla, G Gigliotti, JM Kenny, A Chiralt and L Torre. Production and characterization of PLA_PBS biodegradable blends reinforced with cellulose nanocrystals extracted from hemp fibres. *Industrial Crops and Products* 2016; **93(4)**, 276-289.

[6] P Phanthong, P Reubroycharoen, X Hao, G Xu, A Abudula and G Guan. Nanocellulose: Extraction and application. *Carbon Resources Conversion* 2018; **1(1)**, 32-43.

[7] JD Aguiar, TJ Bondancia, PIC Claro, LHC Mattoso, CS Farinas and JM Marconcini. Enzymatic deconstruction of sugarcane bagasse and straw to obtain cellulose nanomaterials. *ACS Sustainable Chemistry & Engineering* 2020; **8(5)**, 2287-2299.

[8] M Jonoobi, J Harun, AP Mathew and K Oksman. Mechanical properties of cellulose nanofiber (CNF) reinforced polylactic acid (PLA) prepared by twin screw extrusion. *Composites Science and Technology* 2010; **70(12)**, 1742-1747.

[9] E Fortunati, I Armentano, Q Zhou, D Puglia, A Terenzi, LA Berglund and JM Kenny. Microstructure and nonisothermal cold crystallization of PLA composites based on silver nanoparticles and nanocrystalline cellulose. *Polymer Degradation and Stability* 2012; **97(10)**, 2027-2036.

[10] B Wang and LT Drzal. Cellulose nanofiber-reinforced poly(lactic acid) composites prepared by a water-based approach. *ACS Applied Materials & Interfaces* 2012; **4(10)**, 5079-5085.

[11] X Xu, F Liu, L Jiang, JY Zhu, D Haagenson and DP Wiesenborn. Cellulose nanocrystals vs. cellulose nanofibrils: A comparative study on their microstructures and effects as polymer reinforcing agents. *ACS Applied Materials & Interfaces* 2016; **8(4)**, 2349-2359.

[12] N Lin, J Yu, P Chang, J Li and J Huang. Poly(butylene succinate)-based biocomposites filled with polysaccharide nanocrystals: Structure and properties. *Polymer Composites* 2011; **32(3)**, 472-482.

[13] GM DeLoid, X Cao, RM Molina, DI Silva, K Bhattacharya, KW Ng, SCJ Loo, JD Brain and P Demokritou. Toxicological effects of ingested nanocellulose in *in vitro* intestinal epithelium and *in vivo* rat models. *Environmental Science: Nano* 2019; **6(7)**, 2105-2115.

[14] MP Bernardo, BCRD Silva, AEI Hamouda, MASD Toledo, C Schalla, S Rutten, R Goetzke, LHC Mattoso, M Zenke and A Sechi. PLA/Hydroxyapatite scaffolds exhibit *in vitro* immunological inertness and promote robust osteogenic differentiation of human mesenchymal stem cells without osteogenic stimuli. *Scientific Reports* 2022; **12(1)**, 2333.

[15] EM Hietala, US Salminen, A Stahls, T Valimaa, P Maasilta, P Tormala, MS Nieminen and ALJ Harjula. Biodegradation of the copolymeric polylactide stent: Long-term follow-up in a rabbit aorta model. *Journal of Vascular Research* 2001; **38(4)**, 361-369.

[16] M Gigli, M Fabbri, N Lotti, R Gamberini, B Rimini and A Munari. Poly(butylene succinate)-based polyesters for biomedical applications: A review. *European Polymer Journal* 2016; **75**, 431-460.

[17] YS Maigari, M Yakubu, A Atta and M Bukhari. Extraction and characterization of nanocrystalline cellulose powder from corn cob. *The Bangladesh Journal of Scientific Research* 2016; **15(1)**, 50-55.

[18] P Tanthaisong, S Imsoonthornruksa, A Ngernsoungnern, P Ngernsoungnern, M Ketudat-Cairns and R Parnpai. Enhanced chondrogenic differentiation of human umbilical cord wharton's jelly derived mesenchymal stem Cells by GSK-3 inhibitors. *PLoS One* 2017; **12(1)**, e0168059.

[19] W Panta, S Imsoonthornruksa, T Yoisungnern, S Suksaweang, M Ketudat-Cairns and R Parnpai. Enhanced hepatogenic differentiation of human wharton's jelly–derived mesenchymal stem cells by using three-step protocol. *International Journal of Molecular Sciences* 2019; **20(12)**, 3016.

[20] X Hu, T Su, P Li and Z Wang. Blending modification of PBS/PLA and its enzymatic degradation. *Polymer Bulletin* 2018; **75(2)**, 533-546.

[21] N Lin, J Huang, PR Chang, J Feng and J Yu. Surface acetylation of cellulose nanocrystal and its reinforcing function in poly(lactic acid). *Carbohydrate Polymers* 2011; **83(4)**, 1834-1842.

[22] C Endes, S Camarero-Espinosa, S Mueller, EJ Foster, A Petri-Fink, B Rothen-Rutishauser, C Weder and MJD Clift. A critical review of the current knowledge regarding the biological impact of nanocellulose. *Journal of Nanobiotechnology* 2016; **14(1)**, 78.

[23] C Wu, DJ McClements, M He, L Zheng, T Tian, F Teng and Y Li. Preparation and characterization of okara nanocellulose fabricated using sonication or high-pressure homogenization treatments. *Carbohydrate Polymers* 2020; **255**, 117364.

[24] P Squinca, S Bilatto, AC Badino and CS Farinas. Nanocellulose production in future biorefineries: An Integrated approach using tailor-made enzymes. *ACS Sustainable Chemistry & Engineering* 2020; **8(5)**, 2277-2286.

[25] AC O'Sullivan. Cellulose: The structure slowly unravels. *Cellulose* 1997; **4(3)**, 173-207.

[26] RJ Moon, A Martini, J Nairn, J Simonsen and J Youngblood. Cellulose nanomaterials review: Structure, properties, and nanocomposites. *Chemical Society Reviews* 2011; **40(7)**, 3941-3994.

[27] AD French. Idealized powder diffraction patterns for cellulose polymorphs. *Cellulose* 2014; **21(2)**, 885-896.

[28] Y Hishikawa, E Togawa and T Kondo. Characterization of individual hydrogen bonds in crystalline regenerated cellulose using resolved

polarized FTIR spectra. *ACS Omega* 2017; **2(4)**, 1469-1476.

[29] M Makarem, CM Lee, K Kafle, S Huang, I Chae, H Yang, JD Kubicki and SH Kim. Probing cellulose structures with vibrational spectroscopy. *Cellulose* 2019; **26(1)**, 35-79.

[30] A Boukir, I Mehyaoui, S Fellak, L Asia and P Doumenq. The effect of natural degradation process on the cellulose structure of moroccan hardwood fiber: A survey on spectroscopy and structural properties. *Mediterranean Journal of Chemistry* 2019; **8(3)**, 179-190.

[31] R Javier-Astete and G Zolla. Determination of hemicellulose, cellulose, holocellulose and lignin content using FTIR in Calycophyllum spruceanum (Benth.) K. Schum. and Guazuma crinita Lam. *PLoS One* 2021; **16(10)**, e0256559.

[32] RM Salim, J Asik and M Sarjadi. Chemical functional groups of extractives, cellulose and lignin extracted from native Leucaena leucocephala bark. *Wood Science and Technology* 2021; **55**, 295-313.

[33] MH Kudzin, Z Mrozinska and P Urbaniak. Vapor phosphorylation of cellulose by phosphorus trichlo-ride: Selective phosphorylation of 6-hydroxyl function—the synthesis of new antimicrobial cellulose 6-phosphate(III)-copper complexes. *Antibiotics* 2021; **10(2)**, 203.

[34] AE Oudiani, S Msahli and F Sakli. In-depth study of agave fiber structure using Fourier transform infrared spectroscopy. *Carbohydrate Polymers* 2017; **164**, 242-248.

[35] A Parihar, J Vongsvivut and S Bhattacharya. Synchrotron-based infra-red spectroscopic insights on thermo-catalytic conversion of cellulosic feedstock to levoglucosenone and furans. *ACS Omega* 2019; **4(5)**, 8747-8757.

[36] H Wang, M Zuo, N Ding, G Yan, X Zeng, X Tang, Y Sun, T Lei and L Lin. Preparation of nanocellulose with high-pressure homogenization from pretreated biomass with cooking with active oxygen and solid alkali. *ACS Sustainable Chemistry & Engineering* 2019; **7(10)**, 9378-9386.

[37] D Klemm, B Heublein, HP Fink and A Boh. Cellulose: Fascinating biopolymer and sustainable raw material. *Angewandte Chemie International Edition* 2005; **44(22)**, 3358-3393.

[38] D Trache, MH Hussin, MKM Haafiz and VK Thakur. Recent progress in cellulose nanocrystals: Sources and production. *Nanoscale* 2017; **9(5)**, 1763-1768.

[39] G Cheng, X Zhang, B Simmons and S Singh. Theory, practice and prospects of x-ray and neutron scattering for lignocellulosic biomass characterization: Towards understanding biomass pretreatment. *Energy & Environmental Science* 2014; **8(2)**, 436-455.

[40] F Lionetto, R Lopez-Munoz, C Espinoza-Gonzalez, R Mis-Fernandez, O Rodriguez-Fernandez and A Maffezzoli. A study on exfoliation of expanded graphite stacks in candelilla wax. *Materials* 2019; **12(16)**, 2530.

[41] O Nechyporchuk, MN Belgacem and J Bras. Production of cellulose nanofibrils: A review of recent advances. *Industrial Crops and Products* 2016; **93(6)**, 2-25.

[42] G Siqueira, J Bras and A Dufresne. Cellulosic bionanocomposites: A review of preparation, properties and applications. *Polymers* 2010; **2(4)**, 728-765.

[43] A Peciulyte, K Karlstrom, PT Larsson and L Olsson. Impact of the supramolecular structure of cellulose on the efficiency of enzymatic hydrolysis. *Biotechnology for Biofuels* 2015; **8(1)**, 56.

[44] A Tąta, K Sokołowska, J Swider, A Konieczna-Molenda, E Proniewicz and E Witek. Study of cellulolytic enzyme immobilization on copolymers of N-vinylformamide. *Spectrochimica Acta Part A: Molecular and Biomolecular Spectroscopy* 2015; **149**, 494-504.

[45] Y Peng, DJ Gardner and Y Han. Characterization of mechanical and morphological properties of cellulose reinforced polyamide 6 composites. *Cellulose* 2015; **22**, 3199-3215.

[46] L Chen, JY Zhu, C Baez, P Kitin and T Elder. Highly thermal-stable and functional cellulose nanocrystals and nanofibrils produced using fully recyclable organic acids. *Green Chemistry* 2016; **13(8)**, 3835-3843.

[47] S Park, JO Baker, ME Himmel, PA Parilla and DK Johnson. Cellulose crystallinity index:

Measurement techniques and their impact on interpreting cellulase performance. *Biotechnology for Biofuels* 2010; **3(1)**, 10.

[48] G Lutzweiler, AN Halili and NE Vrana. The overview of porous, bioactive scaffolds as instructive biomaterials for tissue regeneration and their clinical translation. *Pharmaceutics* 2020; **12(7)**, 602.

[49] L Jompang, S Thumsorn, J W On, P Surin, C Apawet, T Chaichalermwong, N Kaabbuathong, N O-Charoen and N Srisawat. Poly(lactic acid) and poly(butylene succinate) blend fibers prepared by melt spinning technique. *Energy Procedia* 2013; **34**, 493-499.